Modelling Simul. Mater. Sci. Eng. **17** (2009) 075007 (26pp) doi:10.1088/0965-0393/17/7/075007

Modelling dislocations in a free-standing thin film

Christopher R Weinberger[1], Sylvie Aubry[1], Seok-Woo Lee[2], William D Nix[2] and Wei Cai[1]

[1] Department of Mechanical Engineering, Stanford University, CA 94305-4040, USA
[2] Department of Materials Science and Engineering, Stanford University, CA 94305-4034, USA

Received 26 January 2009, in final form 18 June 2009
Published 14 August 2009
Online at stacks.iop.org/MSMSE/17/075007

Abstract

We present a set of efficient numerical algorithms to accurately compute the forces on dislocations in free-standing thin films. We first present a spectral method for computing the image stress field of dislocations in an isotropic elastic half space and a free-standing thin film. The traction force on the free surface is decomposed into Fourier modes by a discrete Fourier transform and the resulting image stress field is obtained by superimposing analytic solutions in the Fourier space. Dislocations intersecting free surfaces are discussed, including the use of virtual segments and the associated uniqueness of their solutions. The efficiency of the algorithm is enhanced by incorporating the analytical solutions for straight dislocations intersecting free surfaces. A comprehensive algorithm, including a flow diagram, is formulated and the numerical convergence of these algorithms discussed. As a benchmark, we compute the equilibrium orientation of a threading dislocation in a free-standing thin film. Good agreement is observed between the predictions from the dislocation dynamics model and those from molecular static simulations and the line tension model.

1. Introduction

Dislocation dynamics (DD) simulation has the potential to quantitatively link the stress–strain curve of a single crystal with the fundamental dislocation mechanisms, by tracking the evolution of dislocations during plastic deformation [1–8]. The effect of individual dislocations on plasticity becomes even more important for sample sizes at the micro-scale, where the flow stress has been observed to become size dependent [9–15]. DD simulations, once extended to account for free surface effects, will be a first step in understanding the physics behind the size effects. The incorporation of other detailed mechanisms such as: climb, cross-slip, the motion of kinks, jogs and dissociation will further enhance our understanding of plasticity at small scales. However, we leave these details for future research and the focus of this work is on the free surface contributions to dislocation driving forces.

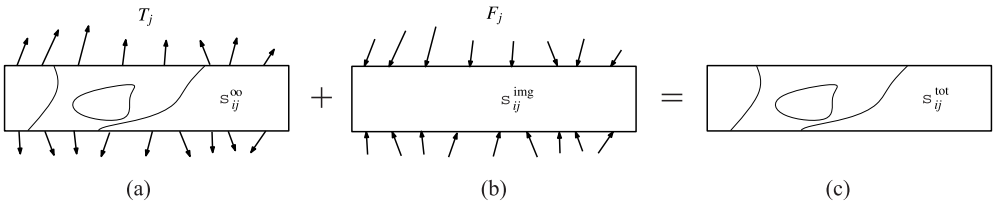

Figure 1. (a) Traction forces T_j on the surface of a dislocated thin film when using σ_{ij}^{∞}. (b) Image stress (σ_{ij}^{img}) produced by the auxiliary problem to cancel the traction forces. (c) The stress field (σ_{ij}^{tot}) of a dislocated, traction-free thin film is obtained by the superposition of σ_{ij}^{∞} and σ_{ij}^{img}.

Accounting for the effects of the free surfaces is not a trivial task because a micro-scale sample can still contain many dislocations, whose interaction with the surface and with each other needs to be accurately accounted for at each time step of the DD simulation. In this paper, we present a complete description of a set of efficient numerical algorithms to compute the image force that arises due to the free surface in free-standing thin films. First, we present a set of spectral methods for computing the image stress in half spaces and thin films using analytical solutions similar to that of elastic cylinders [16]. Second, we discuss the concept of virtual segments, which are needed to make the problem well-posed [8, 17]. Third, we show how the Yoffe solution of a semi-infinite dislocation in an elastic half space [18] can be incorporated to increase the convergence rate of the spectral method. This problem is discussed in detail, including the singular nature of the image stress field at the piercing point. We also present a complete flow diagram of how all of these routines are integrated into a DD program. Finally, we discuss the convergence of the different algorithms and their contributions to the image and total force on dislocations.

2. Problem statement

The standard way to find the stress field for a dislocation inside an elastic medium with surfaces is to start with the stress field of the same dislocation in an infinite medium (σ_{ij}^{∞}) and add an image stress field (σ_{ij}^{img}) to cancel the residual tractions on the surface [7, 8, 19, 20], as illustrated in figure 1. Thus, the total stress inside the medium can be thought of as a superposition of the two stress fields

$$\sigma_{ij}^{\text{tot}} = \sigma_{ij}^{\infty} + \sigma_{ij}^{\text{img}}. \tag{1}$$

Since the interactions of dislocations in an isotropic infinite medium are well known, we are left to compute the image stress field, which is the stress field produced in the medium (such as a free-standing thin film) subjected to an arbitrary distribution of traction forces F_j on the surface. This is a boundary value problem and can be solved by the finite element method (FEM) or the boundary element method (BEM). However, given the special geometry of the free-standing thin film, analytic solutions can be obtained (in Fourier space). Using a discrete Fourier transform (DFT), this can lead to a more efficient way to solve the image stress than the standard FEM or BEM method. A similar approach was taken in solving the image stress in an elastic cylinder [16]. The computational efficiency is critical for DD simulations in thin films because an image stress problem needs to be solved at every time step of the simulation (which may involve a million time steps).

3. Elasticity solution in fourier space

In the absence of body forces, the stress equilibrium of an isotropic linear elastic medium can be written in terms of the displacement field $u_i(\boldsymbol{x})$ as

$$\mu\, u_{i,jj} + (\lambda + \mu)\, u_{j,ji} = 0, \tag{2}$$

where $\lambda = 2\mu\nu/(1-2\nu)$ and μ are the Lamé constants, μ is also the shear modulus and ν is Possion's ratio. The following solution [21] to this equation is periodic in the x- and y-directions and exponential in the z-direction, the normal direction in the film geometry, and is particularly useful for the problem considered here:

$$\begin{aligned}
u_x &= \left(Ak_x z - Bk_y + \mathrm{i}Ck_x\right)\mathrm{e}^{\mathrm{i}k_x x + \mathrm{i}k_y y + k_z z} + \left(Ek_x z + Fk_y + \mathrm{i}Gk_x\right)\mathrm{e}^{\mathrm{i}k_x x + \mathrm{i}k_y y - k_z z},\\
u_y &= \left(Ak_y z + Bk_x + \mathrm{i}Ck_y\right)\mathrm{e}^{\mathrm{i}k_x x + \mathrm{i}k_y y + k_z z} + \left(Ek_y z - Fk_x + \mathrm{i}Gk_y\right)\mathrm{e}^{\mathrm{i}k_x x + \mathrm{i}k_y y - k_z z},\\
u_z &= \left(-\mathrm{i}Ak_z z + \mathrm{i}A\frac{\lambda+3\mu}{\lambda+\mu} + Ck_z\right)\mathrm{e}^{\mathrm{i}k_x x + \mathrm{i}k_y y + k_z z}\left(\mathrm{i}Ek_z z + \mathrm{i}E\frac{\lambda+3\mu}{\lambda+\mu} - Gk_z\right)\mathrm{e}^{\mathrm{i}k_x x + \mathrm{i}k_y y - k_z z},
\end{aligned} \tag{3}$$

where $k_z = \sqrt{k_x^2 + k_y^2}$ and A, B, C and E, F, G are complex constants. The displacements here are written in terms of complex exponentials for use with DFTs. In the end we only take the real part of the solution.

Due to the completeness of the Fourier series, an arbitrary displacement field (satisfying equilibrium) can be written as a superposition of the general solutions written above, each with a different k_x and k_y. For convenience, we write the Fourier components of the displacement field as

$$\begin{aligned}
\hat{u}_x &= \left(Ak_x z - Bk_y + \mathrm{i}Ck_x\right)\mathrm{e}^{+k_z z} + \left(Ek_x z + Fk_y + \mathrm{i}Gk_x\right)\mathrm{e}^{-k_z z},\\
\hat{u}_y &= \left(Ak_y z + Bk_x + \mathrm{i}Ck_y\right)\mathrm{e}^{+k_z z} + \left(Ek_y z - Fk_x + \mathrm{i}Gk_y\right)\mathrm{e}^{-k_z z},\\
\hat{u}_z &= \left(-\mathrm{i}Ak_z z + \mathrm{i}A\frac{\lambda+3\mu}{\lambda+\mu} + Ck_z\right)\mathrm{e}^{+k_z z} + \left(\mathrm{i}Ek_z z + \mathrm{i}E\frac{\lambda+3\mu}{\lambda+\mu} - Gk_z\right)\mathrm{e}^{-k_z z}.
\end{aligned} \tag{4}$$

The total displacement field is then just a sum over the different Fourier modes

$$\boldsymbol{u}(x, y, z) = \sum_{k_x}\sum_{k_y} \hat{\boldsymbol{u}}(k_x, k_y, z)\exp[\mathrm{i}k_x x + \mathrm{i}k_y y]. \tag{5}$$

The stress field can be obtained from displacements, and can also be written in a similar form as

$$\boldsymbol{\sigma}(x, y, z) = \sum_{k_x}\sum_{k_y} \hat{\boldsymbol{\sigma}}(k_x, k_y, z)\ \exp[\mathrm{i}k_x x + \mathrm{i}k_y y]. \tag{6}$$

The above expressions can be used to satisfy either traction or displacement boundary conditions on the surfaces of a thin film or an elastic half space. This can be done on a mode by mode basis by expanding either the tractions or displacements on the surfaces in a Fourier series as well:

$$\boldsymbol{T}(x, y) = \sum_{k_x}\sum_{k_y} \hat{\boldsymbol{T}}(k_x, k_y)\ \exp[\mathrm{i}k_x x + \mathrm{i}k_y y], \tag{7}$$

$$\bar{\boldsymbol{u}}(x, y) = \sum_{k_x}\sum_{k_y} \hat{\bar{\boldsymbol{u}}}(k_x, k_y)\ \exp[\mathrm{i}k_x x + \mathrm{i}k_y y]. \tag{8}$$

The unknown coefficients, A, B, C and E, F, G, can be obtained for each Fourier mode by matching the prescribed traction or displacement. The numerical algorithm for doing this in half spaces and free-standing thin films will be elaborated in the following subsections.

3.1. Elastic half space

Prior to developing the solution that satisfies the boundary condition of a thin film, it is instructive to see how the above solution can be used to solve a simpler problem, that is the stress field in an elastic half space subjected to arbitrary traction on the surface. The solutions developed here will also be useful for the thin film.

We will consider both negative and positive half spaces. Both half spaces will be considered periodic in both the x- and y-directions with periodic lengths L_x and L_y, respectively. The assumptions of periodicity, which will be used throughout this paper, set the wave vectors $k_x = 2\pi n_x/L_x$ and $k_y = 2\pi n_y/L_y$, where $n_x, n_y = 0, \pm1, \pm2, \ldots$.

3.1.1. Solution in the lower half space. Consider an elastic half space that occupies the region $z \leqslant 0$. For the solution to be bounded as $z \to -\infty$, we only keep the terms with $e^{k_z z}$. Hence

$$\begin{aligned}
\hat{u}_x^- &= \left(Ak_x z - Bk_y + \mathrm{i}Ck_x\right) e^{+k_z z},\\
\hat{u}_y^- &= \left(Ak_y z + Bk_x + \mathrm{i}Ck_y\right) e^{+k_z z},\\
\hat{u}_z^- &= \left(-\mathrm{i}Ak_z z + \mathrm{i}A\frac{\lambda+3\mu}{\lambda+\mu} + Ck_z\right) e^{+k_z z}.
\end{aligned} \tag{9}$$

We use the superscript $^-$ to indicate that this solution exists in the domain $z \leqslant 0$. The displacement field on the surface $z = 0$ has the following form

$$\overline{\boldsymbol{u}}(x, y) = \begin{pmatrix} \hat{\bar{u}}_x \\ \hat{\bar{u}}_y \\ \hat{\bar{u}}_z \end{pmatrix} e^{\mathrm{i}k_x x + \mathrm{i}k_y y}, \tag{10}$$

where $\hat{\bar{u}}_x, \hat{\bar{u}}_y, \hat{\bar{u}}_z$ are related to the coefficients A, B, C through the matrix equation

$$\begin{pmatrix} \hat{\bar{u}}_x \\ \hat{\bar{u}}_y \\ \hat{\bar{u}}_z \end{pmatrix} = \left[\boldsymbol{N}^-\right] \begin{pmatrix} A \\ B \\ C \end{pmatrix}. \tag{11}$$

All of the matrices developed here are given in appendix A. From the displacement field in equation (9), it is straightforward to obtain the strain field ϵ_{ij} through differentiation and the stress field σ_{ij} using Hooke's law. The corresponding tractions on the surface $z = 0$ are composed of the stress components $\sigma_{xz}, \sigma_{yz}, \sigma_{zz}$, and must have the following form:

$$\boldsymbol{T}(x, y) = \begin{pmatrix} \hat{T}_x \\ \hat{T}_y \\ \hat{T}_z \end{pmatrix} e^{\mathrm{i}k_x x + \mathrm{i}k_y y}, \tag{12}$$

where $\hat{T}_x, \hat{T}_y, \hat{T}_z$ are related to the coefficients A, B, C through a matrix equation

$$\begin{pmatrix} \hat{T}_x \\ \hat{T}_y \\ \hat{T}_z \end{pmatrix} = \left[\boldsymbol{M}^-\right] \begin{pmatrix} A \\ B \\ C \end{pmatrix}. \tag{13}$$

From these relationships we can determine the Fourier coefficients A, B, C of any Fourier mode (k_x, k_y), given the surface traction $(\hat{T}_x, \hat{T}_y, \hat{T}_z)$ or the surface displacement $(\hat{\bar{u}}_x, \hat{\bar{u}}_y, \hat{\bar{u}}_z)$. Once the Fourier coefficients are obtained, the stress field of this Fourier mode is completely determined through the analytic expressions.

In the general image stress problem, the traction forces are prescribed on the surface, making the $\boldsymbol{M}^-$ matrix appear to be more useful than the $\boldsymbol{N}^-$ matrix. However, it may be advantageous to transform the half space problem to an equivalent problem in an infinite medium, in which an internal stress field is generated by a distribution of body forces, displacement jumps or dislocations on the $z = 0$ interface. The matrix $\boldsymbol{N}^-$ will be useful for this transformation. To do so, we also need the elasticity solution in the upper half space $z \geqslant 0$.

3.1.2. Solution in the upper half space. The Fourier solution that applies to the upper half plane is

$$\begin{aligned}
\hat{u}_x^+ &= \left(Ek_x z + Fk_y + \mathrm{i}Gk_x\right) \mathrm{e}^{-k_z z}, \\
\hat{u}_y^+ &= \left(Ek_y z - Fk_x + \mathrm{i}Gk_y\right) \mathrm{e}^{-k_z z}, \\
\hat{u}_z^+ &= \left(\mathrm{i}Ek_z z + \mathrm{i}E\frac{\lambda + 3\mu}{\lambda + \mu} - Gk_z\right) \mathrm{e}^{-k_z z}.
\end{aligned} \tag{14}$$

The corresponding displacement field on the surface $z = 0$ is related to the Fourier coefficients E, F, G through the matrix equation:

$$\begin{pmatrix} \hat{\bar{u}}_x \\ \hat{\bar{u}}_y \\ \hat{\bar{u}}_z \end{pmatrix} = \left[\boldsymbol{N}^+\right] \begin{pmatrix} E \\ F \\ G \end{pmatrix}. \tag{15}$$

The corresponding traction force on the surface $z = 0$ is related to the Fourier coefficients through the following matrix relation:

$$\begin{pmatrix} \hat{T}_x \\ \hat{T}_y \\ \hat{T}_z \end{pmatrix} = -\left[\boldsymbol{M}^+\right] \begin{pmatrix} E \\ F \\ G \end{pmatrix}. \tag{16}$$

In equation (16) we introduce the minus sign to emphasize the fact that the normal vector of the upper half space is in the $-z$-direction, hence $\hat{T}_x$, $\hat{T}_y$, $\hat{T}_z$ correspond to $-\sigma_{xz}$, $-\sigma_{yz}$, $-\sigma_{zz}$.

3.1.3. Equivalent solutions in an infinite medium. We are now ready to construct a solution in an infinite medium that is equivalent to the solution in a lower half space subjected to a surface traction. The two problems are equivalent in the sense that they have identical displacement, strain and stress fields in the lower half space $z \leqslant 0$. The process of constructing an equivalent problem in an infinite medium can be imagined as putting together two solutions—for the lower and upper half spaces, respectively, as illustrated in figure 2. While the solution in the lower half space has to be identical to the original half space problem, there are several choices for the upper half space solution. We can choose the displacement field to be continuous across the interface $z = 0$ resulting in a jump in the traction forces, which must be balanced by a distribution of body forces. Hence the equivalent problem in the infinite medium is the stress field generated by body forces distributed on the internal interface $z = 0$. Alternatively, we can choose the traction force to be continuous across the interface $z = 0$. Then, there will be a jump in the displacement field, which can be interpreted as a network of dislocations. Hence the equivalent problem in the infinite medium is the stress field generated by a distribution of dislocations on the internal interface $z = 0$. In the following, we give more mathematical details of these two approaches.

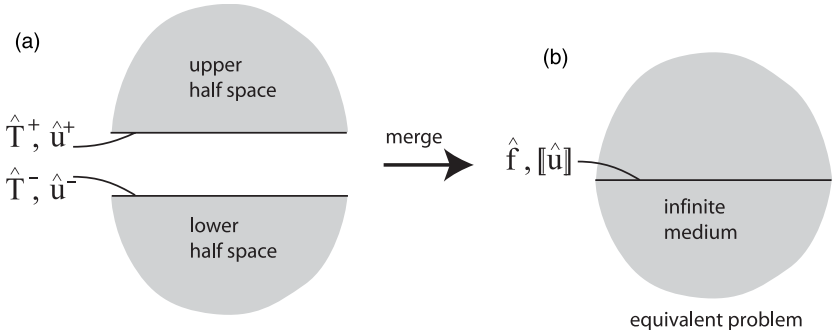

Figure 2. (*a*) A positive and negative half space. (*b*) The union of the two half spaces produces an infinite space.

Let $\hat{\boldsymbol{T}}^-$ and $\boldsymbol{u}^-$ be traction force and displacement field on the surface of the lower half space (consider only a single Fourier mode k_x, k_y). They are related to each other through the $\boldsymbol{M}^-$ and $\boldsymbol{N}^-$ matrices

$$\hat{\boldsymbol{T}}^- = \boldsymbol{M}^-(\boldsymbol{N}^-)^{-1}\hat{\boldsymbol{u}}^-. \tag{17}$$

The traction and displacement fields, $\hat{\boldsymbol{T}}^+$ and $\boldsymbol{u}^+$, on the surface of the upper half space are related to each other through the $\boldsymbol{M}^+$ and $\boldsymbol{N}^+$ matrices

$$\hat{\boldsymbol{T}}^+ = -\boldsymbol{M}^+(\boldsymbol{N}^+)^{-1}\hat{\boldsymbol{u}}^+. \tag{18}$$

In the first approach the displacement jump

$$[\![\hat{\boldsymbol{u}}]\!] \equiv \hat{\boldsymbol{u}}^- - \hat{\boldsymbol{u}}^+ = 0 \tag{19}$$

is continuous on the interface $z = 0$. However, we need to maintain a net force on the interface to satisfy equilibrium. The net force is equivalent to a body force array

$$\hat{\boldsymbol{f}} = \hat{\boldsymbol{T}}^- + \hat{\boldsymbol{T}}^+ = \left(\boldsymbol{M}^-(\boldsymbol{N}^-)^{-1} - \boldsymbol{M}^+(\boldsymbol{N}^+)^{-1}\right)\hat{\boldsymbol{u}}^-. \tag{20}$$

This can be rewritten in terms of traction force exerted on the surface of the lower half space $\hat{\boldsymbol{T}}^-$ as

$$\hat{\boldsymbol{f}} = \left(\boldsymbol{I} - \boldsymbol{M}^+(\boldsymbol{N}^+)^{-1}\boldsymbol{N}^-(\boldsymbol{M}^-)^{-1}\right)\hat{\boldsymbol{T}}^-. \tag{21}$$

Now consider the second approach, in which we require the traction forces on the lower and upper half spaces to cancel each other,

$$\hat{\boldsymbol{f}} = \hat{\boldsymbol{T}}^- + \hat{\boldsymbol{T}}^+ = 0 \tag{22}$$

so that we do not need to apply a body force. In this case, the surface displacements of the two half spaces will not match. The equivalent problem for the infinite medium will have a displacement jump,

$$[\![\hat{\boldsymbol{u}}]\!] = \left(\boldsymbol{N}^-(\boldsymbol{M}^-)^{-1} - \boldsymbol{N}^+(\boldsymbol{M}^+)^{-1}\right)\hat{\boldsymbol{T}}^-. \tag{23}$$

The construction of the equivalent problems in an infinite medium leads to several different approaches to compute the image stress field in the lower half space, such as using the stress field expressions of point force or dislocations in an infinite medium. In a similar study of elastic cylinders, we have found that for equivalent solutions in an infinite medium the stress field of body forces gives the most desirable numerical behavior in the sense that it has both exponential convergence and the weakest singularity [16]. Hence equation (21) is probably the most useful one among the above expressions for computing the image stress. However, as

is illustrated below, equation (23) is needed to compute the image energy. While most of the existing DD simulations do not require the calculation of energies, energy becomes important if we want to study the nucleation of dislocations. In section 5, we use agreement between the image force computed from the image stress and that from the derivative of the image energy to demonstrate the self-consistency of our method.

3.1.4. Energy considerations. The force on a dislocation formally is defined as the negative of the gradient in the elastic energy with respect to the dislocation position. The often used Peach–Koehler force comes from this variation of the energy. Self-consistency of the method demands that the two be equivalent. To test this self-consistency, the energy of the dislocated half space must be determined.

The total stress field was initially decomposed into a sum of the stress field in an infinite medium and the image stress. This approach can be extended to energy as well, thus our total energy is

$$E = E^{\infty} + E^{\text{img}}. \tag{24}$$

The energy we are interested in is the image energy and comes from the difference between the total and infinite energies. It is not the strain energy associated with the image stress. The image energy, following the construction in [16], is

$$\begin{aligned} E^{\text{img}} &= -\tfrac{1}{2}\int_{-L_x/2}^{L_x/2}\int_{-L_y/2}^{L_y/2} \boldsymbol{T}(x,y)\cdot[\![\tilde{\boldsymbol{u}}(x,y)]\!]\,\mathrm{d}x\,\mathrm{d}y \\ &= -\tfrac{1}{2}L_xL_y\sum_{k_x}\sum_{k_y}\hat{\boldsymbol{T}}(k_x,k_y)\cdot[\![\hat{\tilde{\boldsymbol{u}}}]\!](-k_x,-k_y). \end{aligned} \tag{25}$$

The image force on a discretization node $\boldsymbol{r}_i$ of the dislocation is defined through the image energy as

$$\boldsymbol{F}_i^{\text{img}} \equiv -\frac{\partial E^{\text{img}}}{\partial \boldsymbol{r}_i}. \tag{26}$$

For self-consistency, this image force must equal the Peach–Koehler force $\boldsymbol{f}^{\text{img}}$ caused by the image stress $\boldsymbol{\sigma}^{\text{img}}$ integrated over the segments connected to node i,

$$\boldsymbol{f}^{\text{img}}(\boldsymbol{x}) = (\boldsymbol{\sigma}^{\text{img}}\cdot\boldsymbol{b}(\boldsymbol{x}))\times\boldsymbol{\xi}(\boldsymbol{x}), \tag{27}$$

$$\boldsymbol{F}_i^{\text{img}} = \int_L N_i(\boldsymbol{x})\,\boldsymbol{f}^{\text{img}}(\boldsymbol{x})\,\mathrm{d}L(\boldsymbol{x}), \tag{28}$$

where $N_i(\boldsymbol{x})$ is the shape function of node i that goes linearly from 1 at node i to zero at its neighboring nodes, $\boldsymbol{b}(\boldsymbol{x})$ and $\boldsymbol{\xi}(\boldsymbol{x})$ are the Burgers vector and line direction of the dislocation at point $\boldsymbol{x}$ (see [6, 22] for more details).

Self-consistency can be checked, as is done later in the paper, by computing the numerical derivative of the image energy and comparing it with the Peach–Koehler force from the image stress.

3.2. Free-standing thin film

The thin film is assumed to have a thickness of $2t$ in the z-direction and, for convenience, is centered at the origin. Just as we did in the half space problems, we consider a domain that is periodic in both the x- and y-directions.

The Fourier solution of the equilibrium equation in a free-standing thin film $-t \leqslant z \leqslant t$ must contain both $\mathrm{e}^{k_z z}$ and $\mathrm{e}^{-k_z z}$ terms in equation (3). It follows that we have six traction

components and six unknown Fourier coefficients that are related by a 6×6 matrix. This complexity can be avoided by exploiting symmetry and rewriting the Fourier components of displacements in terms of hyperbolic functions. This transforms the problem from a 6×6 problem to two independent 3×3 problems. The new Fourier components of the displacements, which are equivalent to equation (3) with redefined constants, are

$$\hat{u}_x = \left(Ak_x z - Fk_y + \mathrm{i}Gk_x\right)\sinh(k_z z) + \left(Ek_x z + Bk_y + \mathrm{i}Ck_x\right)\cosh(k_z z),$$

$$\hat{u}_y = \left(Ak_y z + Fk_x + \mathrm{i}Gk_y\right)\sinh(k_z z) + \left(Ek_y z - Bk_x + \mathrm{i}Ck_y\right)\cosh(k_z z),$$

$$\hat{u}_z = \left(-\mathrm{i}Ak_z z + \mathrm{i}E\frac{\lambda+3\mu}{\lambda+\mu} + Gk_z\right)\cosh(k_z z) + \left(-\mathrm{i}Ek_z z + \mathrm{i}A\frac{\lambda+3\mu}{\lambda+\mu} + Ck_z\right)\sinh(k_z z).$$

Since the boundary data are prescribed on both the top and bottom surfaces, we choose to distinguish between the two using the superscripts $^+$ and $^-$. Thus, the tractions on the top and bottom surfaces are $\hat{\boldsymbol{T}}^+ = (\hat{T}_x^+, \hat{T}_y^+, \hat{T}_z^+)^{\mathrm{T}}$ and $\hat{\boldsymbol{T}}^- = (\hat{T}_x^-, \hat{T}_y^-, \hat{T}_z^-)^{\mathrm{T}}$, respectively. The displacements on the surfaces are $\hat{\hat{\boldsymbol{u}}}^+ = (\hat{\hat{u}}_x^+, \hat{\hat{u}}_y^+, \hat{\hat{u}}_z^+)^{\mathrm{T}}$ and $\hat{\hat{\boldsymbol{u}}}^- = (\hat{\hat{u}}_x^-, \hat{\hat{u}}_y^-, \hat{\hat{u}}_z^-)^{\mathrm{T}}$ as expected. If we define appropriate linear combinations of these traction and displacement vectors, the problem decouples. This is because the geometry is symmetric under reflection against the x–y plane. Hence the part of the displacement field (involving A, B, C) that is symmetric under the reflection is decoupled from the remaining part (involving E, F, G) that is anti-symmetric under the reflection. The new variables are

$$\hat{\boldsymbol{T}}^{\mathrm{S}} \equiv \frac{1}{2}\begin{pmatrix} \hat{T}_x^+ + \hat{T}_x^- \\ \hat{T}_y^+ + \hat{T}_y^- \\ \hat{T}_z^+ - \hat{T}_z^- \end{pmatrix} = \left[\boldsymbol{M}^{\mathrm{S}}\right]\begin{pmatrix} A \\ B \\ C \end{pmatrix} \tag{29}$$

and

$$\hat{\boldsymbol{T}}^{\mathrm{A}} \equiv \frac{1}{2}\begin{pmatrix} \hat{T}_x^+ - \hat{T}_x^- \\ \hat{T}_y^+ - \hat{T}_y^- \\ \hat{T}_z^+ + \hat{T}_z^- \end{pmatrix} = \left[\boldsymbol{M}^{\mathrm{A}}\right]\begin{pmatrix} E \\ F \\ G \end{pmatrix} \tag{30}$$

for the tractions and

$$\hat{\hat{\boldsymbol{u}}}^{\mathrm{S}} \equiv \frac{1}{2}\begin{pmatrix} \hat{\hat{u}}_x^+ + \hat{\hat{u}}_x^- \\ \hat{\hat{u}}_y^+ + \hat{\hat{u}}_y^- \\ \hat{\hat{u}}_z^+ - \hat{\hat{u}}_z^- \end{pmatrix} = \left[\boldsymbol{N}^{\mathrm{S}}\right]\begin{pmatrix} A \\ B \\ C \end{pmatrix} \tag{31}$$

and

$$\hat{\hat{\boldsymbol{u}}}^{\mathrm{A}} \equiv \frac{1}{2}\begin{pmatrix} \hat{\hat{u}}_x^+ - \hat{\hat{u}}_x^- \\ \hat{\hat{u}}_y^+ - \hat{\hat{u}}_y^- \\ \hat{\hat{u}}_z^+ + \hat{\hat{u}}_z^- \end{pmatrix} = \left[\boldsymbol{N}^{\mathrm{A}}\right]\begin{pmatrix} E \\ F \\ G \end{pmatrix} \tag{32}$$

for the displacements. The explicit expressions for the 3×3 matrices $\boldsymbol{M}^{\mathrm{S}}$, $\boldsymbol{M}^{\mathrm{A}}$, $\boldsymbol{N}^{\mathrm{S}}$ and $\boldsymbol{N}^{\mathrm{A}}$ are given in appendix A. The tractions on the top and bottom surfaces are combined to construct $\hat{\boldsymbol{T}}^{\mathrm{S}}$ and $\hat{\boldsymbol{T}}^{\mathrm{A}}$. The six unknown coefficients are then solved from the inverse of matrices $\boldsymbol{M}^{\mathrm{S}}$ and $\boldsymbol{M}^{\mathrm{A}}$. Given the Fourier coefficients, we can determine the stress at any point.

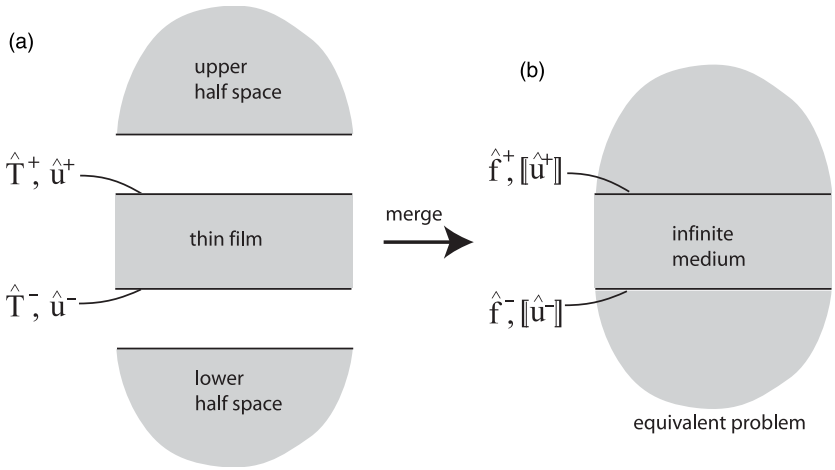

Figure 3. (*a*) An upper and lower half space and a thin film. (*b*) The union of the three domains produces an infinite space.

3.2.1. Equivalent solutions in an infinite medium and energy. The solutions in an equivalent infinite medium for the thin film follow those developed for the half spaces. The idea remains essentially the same as the half space solution in that we think of combining a thin film with two half spaces to form an infinite medium, as illustrated in figure 3.

The resulting solution in the infinite medium is equivalent to our original problems as long as the elastic fields in the infinite medium within the domain $-t \leqslant z \leqslant t$ coincide with the fields in the thin film. Therefore, there are multiple choices to the solutions in the elastic half space and, as a result, how the two half spaces and the thin film join together. One possibility is to require the displacement field to be continuous across the interfaces $z = \pm t$, in which case body forces $\hat{\boldsymbol{f}}^{+}$ and $\hat{\boldsymbol{f}}^{-}$ need to be applied at the top and bottom interfaces to satisfy equilibrium. Alternatively, we can require the stress field to be continuous across the interfaces, in which case there will be displacement jumps $[\![\hat{\boldsymbol{u}}^{+}]\!] \equiv \hat{\boldsymbol{u}}(z = t + 0^{-}) - \hat{\boldsymbol{u}}(z = t + 0^{+})$ and $[\![\hat{\boldsymbol{u}}^{-}]\!] \equiv \hat{\boldsymbol{u}}(z = -t + 0^{+}) - \hat{\boldsymbol{u}}(z = -t + 0^{-})$ at the top and bottom interfaces, respectively.

Again we can create symmetric and anti-symmetric linear combinations of the equivalent body forces (leading to $\hat{\boldsymbol{f}}^{\mathrm{S}}$ and $\hat{\boldsymbol{f}}^{\mathrm{A}}$) and displacement jumps (leading to $[\![\hat{\boldsymbol{u}}^{\mathrm{S}}]\!]$ and $[\![\hat{\boldsymbol{u}}^{\mathrm{A}}]\!]$), similar to those of traction forces and displacement fields. They can be expressed in terms of the symmetric and anti-symmetric part of the traction forces ($\hat{\boldsymbol{T}}^{\mathrm{S}}$ and $\hat{\boldsymbol{T}}^{\mathrm{A}}$) applied to the original thin film:

$$\hat{\boldsymbol{f}}^{\mathrm{S}} = \left(\boldsymbol{I} - \boldsymbol{M}^{+}(\boldsymbol{N}^{+})^{-1}\boldsymbol{N}^{\mathrm{S}}(\boldsymbol{M}^{\mathrm{S}})^{-1}\right)\hat{\boldsymbol{T}}^{\mathrm{S}}, \tag{33}$$

$$\hat{\boldsymbol{f}}^{\mathrm{A}} = \left(\boldsymbol{I} - \boldsymbol{M}^{+}(\boldsymbol{N}^{+})^{-1}\boldsymbol{N}^{\mathrm{A}}(\boldsymbol{M}^{\mathrm{A}})^{-1}\right)\hat{\boldsymbol{T}}^{\mathrm{A}}, \tag{34}$$

$$[\![\hat{\boldsymbol{u}}^{\mathrm{S}}]\!] = \left(\boldsymbol{N}^{\mathrm{S}}(\boldsymbol{M}^{\mathrm{S}})^{-1} - \boldsymbol{N}^{+}(\boldsymbol{M}^{+})^{-1}\right)\hat{\boldsymbol{T}}^{\mathrm{S}}, \tag{35}$$

$$[\![\hat{\boldsymbol{u}}^{\mathrm{A}}]\!] = \left(\boldsymbol{N}^{\mathrm{A}}(\boldsymbol{M}^{\mathrm{A}})^{-1} - \boldsymbol{N}^{+}(\boldsymbol{M}^{+})^{-1}\right)\hat{\boldsymbol{T}}^{\mathrm{A}}. \tag{36}$$

Given the traction forces on the top and bottom surfaces of the original thin film problem, $\hat{\boldsymbol{T}}^{+}$ and $\hat{\boldsymbol{T}}^{-}$, the image energy can be obtained with the following approach. First, from $\hat{\boldsymbol{T}}^{+}$ and $\hat{\boldsymbol{T}}^{-}$ we form symmetrized force components $\hat{\boldsymbol{T}}^{\mathrm{S}}$ and $\hat{\boldsymbol{T}}^{\mathrm{A}}$. Then we obtain the symmetrized displacement jump components $[\![\hat{\boldsymbol{u}}^{\mathrm{S}}]\!]$ and $[\![\hat{\boldsymbol{u}}^{\mathrm{A}}]\!]$ from equations (35) and (36).

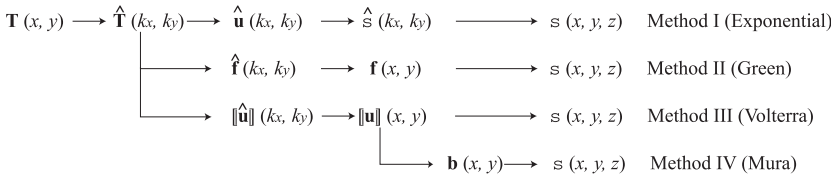

Figure 4. Algorithm flow diagram for computing image stress of a dislocation in a free-standing thin film (no emerging dislocation).

The displacement jumps at the top and bottom interfaces are then obtained from

$$[\![\hat{\tilde{\boldsymbol{u}}}^{+}]\!] = \begin{pmatrix} [\![\hat{\tilde{u}}_x^{\mathrm{S}}]\!] + [\![\hat{\tilde{u}}_x^{\mathrm{A}}]\!] \\ [\![\hat{\tilde{u}}_y^{\mathrm{S}}]\!] + [\![\hat{\tilde{u}}_y^{\mathrm{A}}]\!] \\ [\![\hat{\tilde{u}}_z^{\mathrm{S}}]\!] + [\![\hat{\tilde{u}}_z^{\mathrm{A}}]\!] \end{pmatrix}, \tag{37}$$

$$[\![\hat{\tilde{\boldsymbol{u}}}^{-}]\!] = \begin{pmatrix} [\![\hat{\tilde{u}}_x^{\mathrm{S}}]\!] - [\![\hat{\tilde{u}}_x^{\mathrm{A}}]\!] \\ [\![\hat{\tilde{u}}_y^{\mathrm{S}}]\!] - [\![\hat{\tilde{u}}_y^{\mathrm{A}}]\!] \\ -[\![\hat{\tilde{u}}_z^{\mathrm{S}}]\!] + [\![\hat{\tilde{u}}_z^{\mathrm{A}}]\!] \end{pmatrix}. \tag{38}$$

Finally, the image energy is

$$\begin{aligned} E^{\mathrm{img}} &= -\frac{1}{2}\int_{-L_x/2}^{L_x/2}\int_{-L_y/2}^{L_y/2}\left(\boldsymbol{T}^{+}(x,y)\cdot[\![\bar{\boldsymbol{u}}^{+}(x,y)]\!] + \boldsymbol{T}^{-}(x,y)\cdot[\![\bar{\boldsymbol{u}}^{-}(x,y)]\!]\right)\mathrm{d}x\,\mathrm{d}y \\ &= -\frac{1}{2}L_xL_y\sum_{k_x}\sum_{k_y}\left(\hat{\boldsymbol{T}}^{+}(k_x,k_y)\cdot[\![\hat{\tilde{\boldsymbol{u}}}^{+}]\!](-k_x,-k_y) + \hat{\boldsymbol{T}}^{-}(k_x,k_y)\cdot[\![\hat{\tilde{\boldsymbol{u}}}^{-}]\!](-k_x,-k_y)\right) \end{aligned} \tag{39}$$

4. Algorithm for image force calculation

4.1. Non-emerging dislocations

The above derivations provide several methods to compute the image stress in a thin film containing dislocations. In this section, we give more details on these methods (I–IV) from an algorithm standpoint. Method I uses the analytical formulae for the stress. Methods II, III and IV come from the real space solutions involving body forces and Green functions. Method II computes the stress field from the given distribution of body forces using the elastic Green function. Method III computes the stresses directly from the distribution of displacement jumps using Volterra's formula. Method IV computes the stresses from dislocations between the displacement jumps. A simple flow diagram for methods I–IV is given in figure 4. As a check of self-consistency, we compute the Peach–Koehler force generated by the image stress and compare it with the image force obtained from taking the numerical derivative of the image energy.

The first step for any of the methods is the calculation of the traction matrices. In a DD code, the residual tractions on the thin film surfaces are computed from the dislocation segments using the stress field in an infinite medium. For our algorithm, this is done on a regular rectangular grid of dimensions $L_x \times L_y$. The Fourier components of the tractions, $\hat{\boldsymbol{T}}$, are needed in all methods and are computed by a DFT.

In method I, each Fourier component of the tractions is used to determine the unknown coefficients, A, B, C and E, F, G. From this, the Fourier components of the stress can be determined from the displacements. The total stress field is then a sum of each mode, which must be evaluated at a given point (x, y, z).

Method II requires the construction of equivalent body forces in real space; the expressions for these are given in equation (33). The real space body forces are obtained by a DFT of the Fourier components. From this distribution, the stress field of the body forces can be obtained from the elastic Green function.

$$\sigma_{ij}(\boldsymbol{x}) = \int_S C_{ijkl}\, G_{km,l}(\boldsymbol{x} - \boldsymbol{x}')\, f_m(\boldsymbol{x}')\, \mathrm{d}\boldsymbol{x}'. \tag{40}$$

The integral is carried out over the top and bottom surfaces of the thin film. The simplest method of calculating the stress field is to approximate the distribution as constant over a small area with the magnitude equal to the real space value at that point. Further assuming that the field point is far away from the point force, the integral can be dropped and the stress field is simple to evaluate. This method is shown to work well in [16].

The distribution of displacement jumps in equations (35) and (36) is used in both methods III and IV. For both these methods, the Fourier distribution of displacement jumps is transformed back to give a real space distribution. Method III uses the displacement jumps to compute the stress using Volterra's formula

$$\sigma_{ij}(\boldsymbol{x}) = \int_S C_{ijkl} C_{pqrs}\, n_s\, G_{kp,ql}(\boldsymbol{x} - \boldsymbol{x}')\, [\![u]\!]_r(\boldsymbol{x}')\, \mathrm{d}\boldsymbol{x}'. \tag{41}$$

Just as in method II, the integral is dropped assuming the displacement jumps act at the real space grid points and are multiplied by the area over which they act.

Method IV takes one further step by converting the displacement jumps into dislocations. Since dislocations are lines that bound areas between which there is a difference in displacement jumps, we can approximate the displacement jump distribution from method III with a network of dislocations. The network of dislocations forms a rectangular grid between the real space grid points where the displacement jumps have been evaluated. The Burgers vector of each dislocation is simply the difference between the two displacement jumps that the dislocation divides [16]. This allows us to compute the stress field at a field point from the network of dislocations using the stress fields already available in the DD codes. Given the image stress, we can obtain the image Peach–Koehler force on the dislocation line and image forces on the discretization nodes using equations (27) and (28).

As a check for self-consistency, we can also compute the image force on a network of dislocations from the image energy. The image force defined in equation (26) can be computed by using a simple finite difference scheme, for example

$$\boldsymbol{F}_i^{\mathrm{img}} \approx \frac{E^{\mathrm{img}}(\boldsymbol{r}_i + \boldsymbol{\Delta r}) - E^{\mathrm{img}}(\boldsymbol{r}_i - \boldsymbol{\Delta r})}{2\boldsymbol{\Delta r}}. \tag{42}$$

Therefore, we need to evaluate the energy twice for every force component we wish to determine. This is done by displacing the dislocation by $\boldsymbol{\Delta r}$ in both directions and evaluating the image energy. The image energy from equation (39) at each point is evaluated from the tractions based on the new dislocation position and the displacement jumps from equations (35) and (36).

4.2. Emerging dislocations

4.2.1. Virtual segments. In our preceding discussions, we have neglected the possibility that the dislocation might intersect a free surface. From the image stress problem statement,

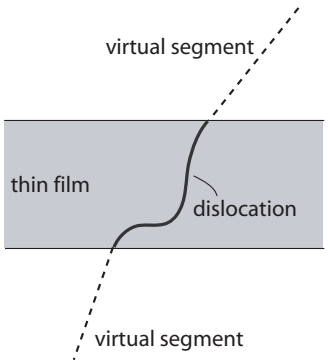

Figure 5. An emerging dislocation in thin film and the semi-infinite virtual segments that continue it in an infinite medium.

the tractions we are trying to negate on the surface come from dislocations in an infinite medium. However, dislocations cannot terminate inside an infinite body. While stress fields of dislocation segments do exist, they only satisfy equilibrium if they form a complete loop, which includes dislocations that continue to infinity. Therefore, if we wish to compute the stress fields due to dislocations that intersect the free surface we must continue them outside the thin film [23], as illustrated in figure 5. These continuations, which are termed *virtual dislocations* [8, 17], allow the dislocation to form a complete loop (or go to infinity) and allow the stress field to satisfy equilibrium. The image stress, then, must account for the surface traction generated by all the real dislocations as well as virtual dislocations.

There are an infinite number of ways to continue a dislocation that intersects the free surface and the stress in the infinite medium, σ_{ij}^{∞}, depends on this configuration. Therefore, the image stress, σ_{ij}^{img}, will be different for different virtual segments. However, the total stress, σ_{ij}^{tot}, will be the same, regardless of configuration, for simply connected bodies such as a thin film. This is because of the uniqueness of the associated boundary value problem, and is shown in appendix B. For our simulations, we choose to continue the dislocations outside the thin film as semi-infinite straight dislocations that are tangent to the dislocation segment intersecting the free surface. This choice is made mainly out of convenience, but it also appears to have the best convergence when the image force is computed using our spectral methods (see numerical results below). The stress fields of semi-infinite dislocations are given in [24, 25].

In DD simulations, the force on the discretization nodes is a sum of the contributions from each of its segments. The force from each segment comes from the integration of the total stress field over that segment and nodal forces are sums of forces from all segments attached to the node. Discretization nodes that lie on the surface will have at least one segment inside the domain and one outside the domain. Since the virtual segments are only a construct to create the correct stress field, the segment forces from virtual segments should not contribute to the nodal force. For this reason, the Peach–Koehler force on the virtual segments must be excluded from the force on the surface node in the simulations. However, since the virtual segments influence both σ_{ij}^{∞} and σ_{ij}^{img}, they need to be included when computing the forces on every node.

4.2.2. Yoffe image stress. In order to obtain tractions on the boundaries, we have to compute σ_{ij}^{∞} at the free surfaces discretized by a grid. This can be a problem for emerging dislocations since the stress field is singular at the piercing point. First, the convergence of the image stress

routine will be slow because of the singularity. Second, if the piercing point and sampling point are close enough, the computed stress values will diverge. Therefore, it is desirable to remove the singularity by superimposing another stress field that satisfies equilibrium and precisely cancels the singularity. To do this, we adopt the method of Tang *et al* [26], where the image stress from Yoffe's solution of a semi-infinite dislocation in a half space is used. The spectral method then only needs to handle the difference between the actual image stress (in the thin film) and the Yoffe image stress solution, which is a non-singular function.

It is interesting to note that the placement of the Yoffe image stress in the algorithm is very similar to that of the virtual segments. First, we start with a 'trial' solution, which is a stress field that satisfies equilibrium but may have residual tractions on the boundary. We let this trial solution be $\sigma_{ij}^{\infty} + \sigma_{ij}^{\mathrm{Y,img}}$, where σ_{ij}^{∞} is the stress field of the dislocation in an infinite medium and $\sigma_{ij}^{\mathrm{Y,img}}$ is the Yoffe image stress. This sum is non-singular at the piercing points, resulting in non-singular tractions on free surfaces. Therefore, the Yoffe image stress contributes to the tractions, T_j, that need to be cancelled by the (numerical, non-singular) image stress. This means that the Yoffe image stress influences T_j and the image stress numerically computed by the spectral method, $\sigma_{ij}^{\mathrm{N,img}}$, in the same way as the virtual segments. To construct the total stress in the thin film, we need to superimpose the trial solution $\sigma_{ij}^{\infty} + \sigma_{ij}^{\mathrm{Y,img}}$ and the numerical image solution $\sigma_{ij}^{\mathrm{N,img}}$ obtained by the spectral method. In other words, the image stress in equation (27) is now decomposed into two components,

$$\boldsymbol{\sigma}^{\mathrm{img}} = \boldsymbol{\sigma}^{\mathrm{Y,img}} + \boldsymbol{\sigma}^{\mathrm{N,img}}. \tag{43}$$

Thus, the Yoffe image stress contributes to the Peach–Koehler forces on the 'real' segments inside the thin film in the same way as the virtual segment does.

4.2.3. Algorithm flow diagram. To model a free-standing film, the DD algorithm originally designed for bulk simulations needs to be modified to account for the surface effect on the Peach–Koehler forces. The flow diagram in figure 6 illustrates how all the various components described above fit together in the final algorithm. Every box between input and output corresponds to an operation. The arrows indicate the dependence of data. The operation downstream depends on the data produced by the operation upstream. The image force $\boldsymbol{F}_i^{\mathrm{img}}$ is computed by numerical integration of equation (28), with $\boldsymbol{f}^{\mathrm{img}}(\boldsymbol{x})$ defined in equation (27) and $\boldsymbol{\sigma}^{\mathrm{img}}$ defined in equation (43). In this paper, we use only one quadrature point at the mid-point of the segment for the numerical integration. As a result, the numerical value of the image force on the surface node is finite even though the image stress is singular at the surface node.

5. Numerical results

In the following we will discuss the numerical results obtained from the algorithms described above. We show the convergence behavior of both the half space and the thin film. Using the half space as an example, we show that the spectral method can produce numerically converged results, even without using the Yoffe image stress solution. On the other hand, the numerical result becomes incorrect when the virtual segment is not included.

5.1. Non-emerging dislocations

The first numerical benchmark is to compute the force on a dislocation array in a half space. We specify a dislocation array because our image stress routines require periodicity in both

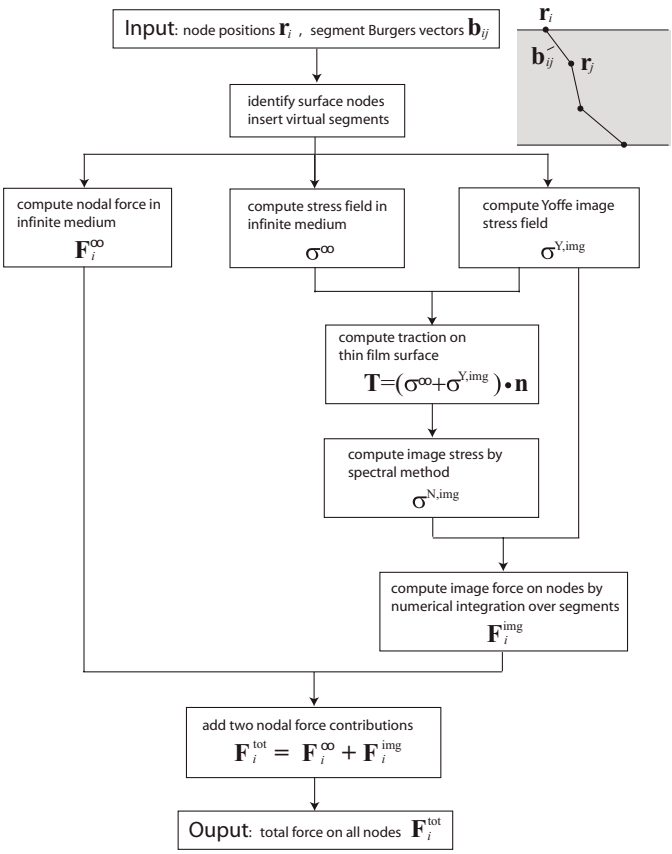

Figure 6. Algorithm flow diagram for computing image stress of a dislocation in a free-standing thin film (with emerging dislocation).

directions in the plane of the surface. The solutions for an array of screw and edge dislocations in an infinite medium are well known [25] and can easily be used to construct the image force of these arrays near a surface.

Figure 7(*a*) shows the relative error in the image force on both an edge and a screw dislocation array in a half space while figure 7(*b*) shows the relative error of a screw array in a thin film. The image forces are computed by the Peach–Koehler formula from the image stresses, which are obtained from Method I in figure 4. To provide a benchmark, analytical formulae for the image force can be obtained from [25]. These figures also show the image force computed from the numerical derivative of the energy, using the finite difference scheme from equation (42). The parameters are $b = 1$, $\mu = 1$, $\nu = 0.3$, $L_x = L_y = 1$ for both plots. For the half space, the dislocations are at a depth $d = 0.1$ below the surface while in the thin film the depth $d = 0.05$ with a thickness $2t = 0.2$.

All numerical results show exponential convergence as $n_x = n_y$ is increased. The error for method I decreases until machine precision is reached for the half space but not the thin film. The slope in the thin film case is also smaller, indicating slower convergence. This is most likely because the dislocation in the thin film is closer to the surface and thus converges slower. The error from the derivative of the energy is generally higher than that from the stress, due to additional numerical error introduced by the finite difference approximation.

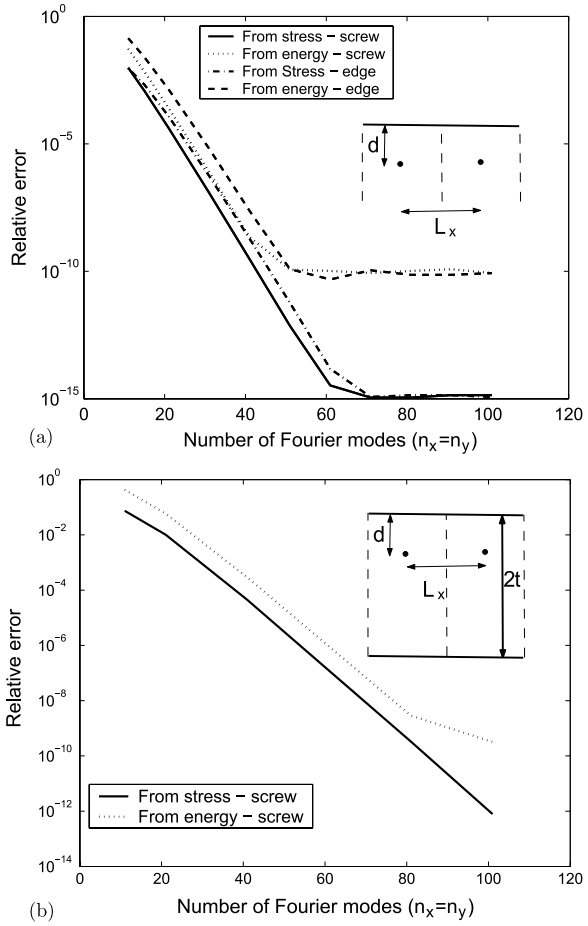

Figure 7. The relative error in computing the image force for dislocation arrays (*a*) in a half space and (*b*) in a thin film. The image force are computed both by using the Peach–Koehler (PK) formula from the image stress and by numerical differentiation of the image energy.

While the above test cases are effectively two dimensional, in the next test case we compute the image stress of a prismatic dislocation loop in a half space and a thin film. Figure 8(*a*) shows the convergence of the numerical result for the half space as a function of the size of the surface grid ($n_x = n_y$), and compares it against the analytical solution [27]. The half space is assumed to be periodic over a distance $L_x = L_y = 1$ with elastic properties $\mu = 1$, $\nu = 0.3$. The loop has a radius $R = 0.1$, a Burgers vector $b = 1$ and is located at a depth $d = 0.1$ below the surface. The circular loop is approximated by a polygonal loop with 500 equally spaced nodes and the force plotted is the component normal to the surface, averaged over all the nodes. Figure 8(*b*) shows the convergence of the numerical result for the thin film, with different thicknesses of the film. The loop is always located at a depth $d = 0.1$ below the surface. As the film thickness increases, the force on the dislocation loop converges to the value for the half space, as expected. Both plots show that the force is well converged at around $n_x = 20$, for which the error is less than 0.1% of its final value. When the depth d is decreased, the minimum spacing between surface grid points should decrease proportionally to obtain the same accuracy.

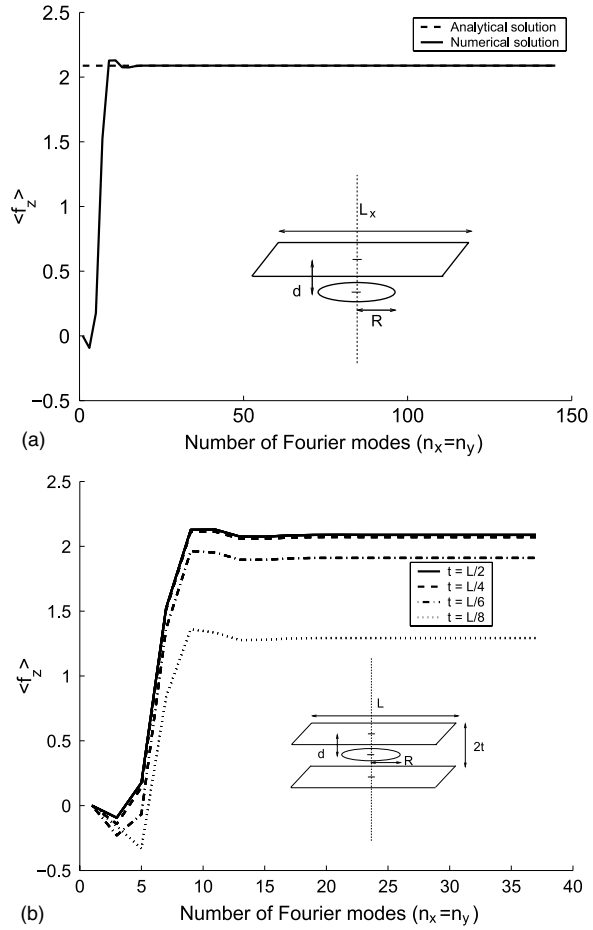

Figure 8. The average image force on a prismatic dislocation loop (*a*) in a half space and (*b*) in a thin film as a function of the size of the surface grid ($n_x = n_y$).

5.2. Emerging dislocation in half space

We have discussed emerging dislocations at length in this paper and provided a few ways of handling them in DD simulations. To provide numerical confirmation of our arguments, figure 9(*a*) plots the total Peach–Koehler force per unit length for a point near the surface on a dislocation emerging from a half space and figure 9(*b*) shows the corresponding image force. Here the image stress is solved by the spectral method alone, without the help of the Yoffe image stress solution. Instead, the Yoffe image stress solution is used as a benchmark to the numerical result. The half space has dimensions $L_x = L_y = 1$ with elastic properties $\mu = 1$ and $\nu = 0.3$. The dislocation line is perpendicular to the surface and the Burgers vector is $\boldsymbol{b} = [1\,0\,1]/\sqrt{2}$. The dislocation intersects the surface at the origin. The Peach–Koehler force is evaluated at a point $(0, 0, z)$ beneath the surface. The Yoffe image stress solution predicts that the Peach–Koehler force simply scales as $1/z$. However, because the spectral method assumes periodicity in the x- and y-directions, the numerical result is only expected to agree with the (Yoffe) analytic solution when $|z|$ is much less than L_x and L_y. In this test case, the Peach–Koehler force is evaluated at $z = -L_x/100$.

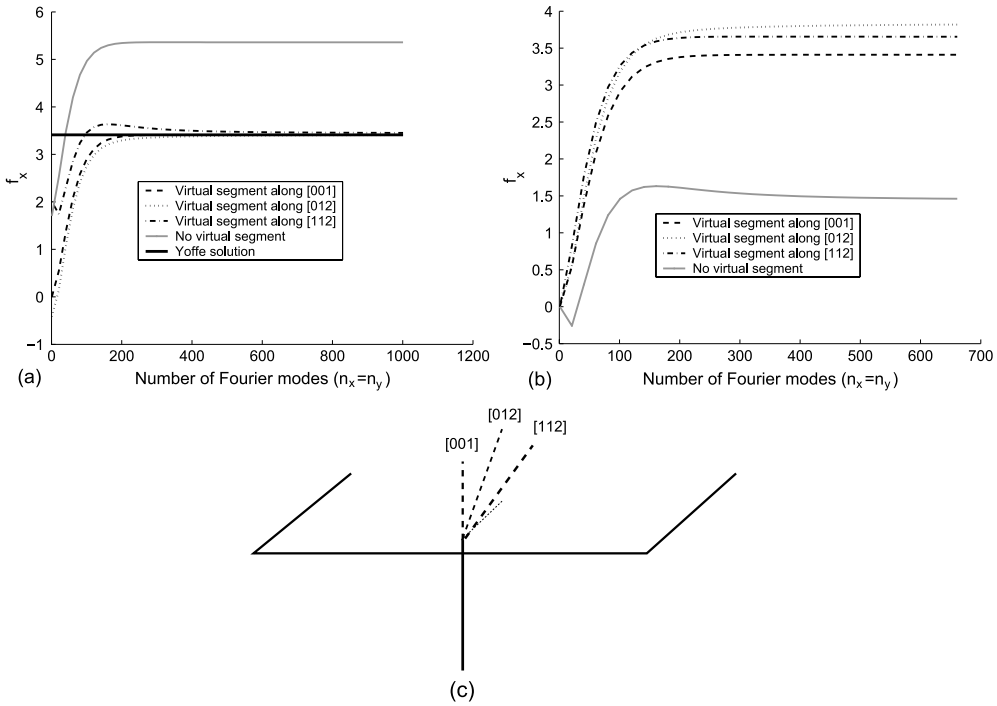

Figure 9. The force on a dislocation emerging from a half space using only the spectral image stress routines for a negative half space. (*a*) The total force on the dislocation from DD simulations with different virtual segments, and from the Yoffe image solution. (*b*) The image force from DD simulations. (*c*) The geometry of the half space, dislocation line and different possible virtual segments.

Figure 9(*a*) clearly illustrates the uniqueness of the total force with respect to the orientation of the virtual segments, whereas figure 9(*b*) shows that the image force is not unique. As the number of surface grids is increased, the total Peach–Koehler force on the dislocation converges to the same analytic solution for three different choices of virtual segment orientations. If the virtual segment is not included in the calculation, the numerical result converges to a wrong value. This clearly illustrates the need to include the virtual segment in the calculation. It is interesting to note that the spectral method can produce results that converge to the analytic solution in the brute-force approach, i.e. by increasing n_x and n_y. In a previous study of a similar geometry using the FEM, the numerical result cannot converge to the analytic solution before the maximum memory of the workstation is exceeded [28]. This is most likely because the spectral method only requires a two-dimensional mesh, while the FEM requires a three-dimensional mesh, which takes up more memory.

5.3. Threading dislocations in thin film

In this section, we compute the equilibrium angle of a dislocation in a free-standing thin film, as a function of the orientation of the Burgers vector. Predictions made from DD simulations will be compared with those from molecular statics (MSs) simulations and the line tension model.

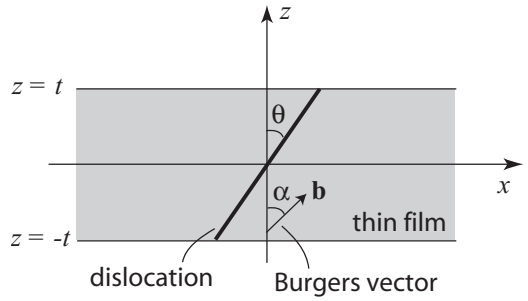

Figure 10. A straight threading dislocation line in a free-standing thin film of thickness $2t$. The angle between the dislocation line and surface normal is θ. The angle between the Burgers vector and surface normal is α.

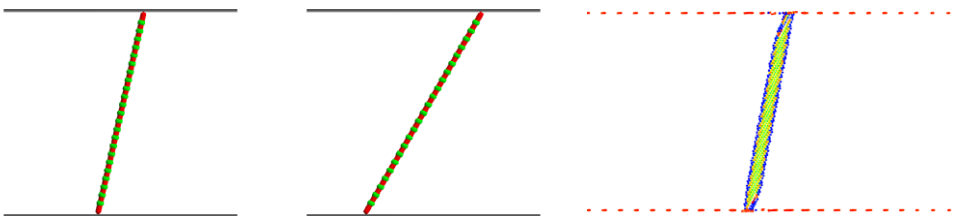

Figure 11. Equilibrium shape of dislocation in a tungsten thin film by (a) DD simulations accounting for the image stress (b) DD simulations ignoring the image stress and (c) MS simulations. The surface normal of the thin film is $\boldsymbol{n} = [1\,\bar{1}\,0]$ and Burgers vector is $\boldsymbol{b} = (a/2)[1\,1\,1]$, which corresponds to an angle of $\alpha = 27.2^\circ$ between $\boldsymbol{b}$ and $\boldsymbol{n}$. The film thickness is $2t = 130.4$ nm in (a) and (b) and $2t = 20$ nm in (c).

(This figure is in colour only in the electronic version)

The behavior of dislocations in thin films has been widely studied in [29–34]. The interest lies in accurately interpreting the image of high resolution transmission electron microscopy (HRTEM) when dislocations are not perpendicular to the surface. The interpretation becomes difficult when the orientation of the dislocation is unknown. In this section, we test whether DD simulations can accurately predict equilibrium dislocation orientation in a free-standing thin film by comparing it with atomistic simulations. Because our DD model is based on isotropic elasticity, we choose to study dislocations in BCC tungsten, which is elastically isotropic. In addition, dislocations in BCC metals do not dissociate, which removes the additional complexity of partial dislocations in FCC metals.

Consider a threading dislocation in an isotropic elastic thin film, as shown in figure 10. Let both the dislocation line and Burgers vector be in the x–z plane, which is also the glide plane of the dislocation. For simplicity, we assume the dislocation remains straight. This assumption will be verified later by the simulation results. Let θ be the angle between the dislocation line and the surface normal (z-axis) and let α be the angle between the Burgers vector and the surface normal. When no external stress is applied, and if we allow the dislocation to go to its equilibrium (i.e. minimum energy) state, the line orientation θ is a function of the orientation of the Burgers vector α.

Figure 11 shows the equilibrium shape of the dislocation in a tungsten thin film predicted by both DD simulations and MS simulations. The shear modulus is $\mu = 16$ GPa and Poisson's

ratio is $\nu = 0.28$, which are chosen to match the Finnis–Sinclair potential [35] used in the MS simulations. In both DD and MS simulations, the Burgers vector is $\boldsymbol{b} = (a/2)[1\,1\,1]$ and the surface normal is $n = [1\,\bar{1}\,0]$ (in crystal coordinate system), where $a = 3.16\,\text{Å}$ is the lattice constant of tungsten. This corresponds to an angle of $\alpha = 27.2^\circ$ between $\boldsymbol{b}$ and $\boldsymbol{n}$. The dislocation line is initialized to be perpendicular to the surface and is then allowed to relax to its equilibrium shape. In DD simulations, the dislocation line is discretized into 25 equally spaced nodes. The periodic lengths in the x- and y-directions are 4 times the film thickness. The grid size for the spectral method is $n_x = n_y = 101$, and Yoffe image stress is applied to remove the surface singularity. The nodes are confined to move along the x-axis with a velocity proportional to the nodal force. This corresponds to the steepest descent algorithm in energy minimization. In MS simulations, the atoms are relaxed to a local energy minimum state by the conjugate gradient algorithm. More details of the MS simulations are given in appendix C.

The efficiency of the spectral method is analyzed in the case of a threading dislocation with a Burgers vector making a 64.7° angle with its initial line direction. The dislocation line is discretized by 25 nodes and the simulation is performed for 4000 time steps, which is typical for reaching the optimal orientation using the spectral method alone. On a Linux 2.4 GHz workstation, the calculations took 74 and 1375 s to complete, when the number of Fourier modes ($n_x = n_y$) is 11 and 101, respectively. As n_x increases from 11 to 101, the time to compute traction forces on the thin film surface increases from 20% of the total computation time to 67%. The time to execute the remaining part of the spectral method, including evaluating the image force on the dislocation nodes, increases from 8% to 30% of the total computation time. Similar results are found when the dislocation is discretized by five nodes. These results show that for a large number of Fourier modes, the code spends a majority of the time on computing the surface tractions and a significant amount of time executing the rest of the spectral method.

The equilibrium dislocation structure from both DD and MS simulations is close to a straight line, confirming the earlier hypothesis. The equilibrium angle θ is obtained by fitting the coordinates of the dislocation nodes (in DD) and dislocation core atoms (in MS) to a straight line. When the image stress is accounted for, the equilibrium orientation θ of the dislocation line predicted by the DD simulation agrees well with the MS simulation. On the other hand, significant discrepancy is observed when the image stress is ignored in the DD simulation, which underlines the importance of image stress in determining the equilibrium dislocation shape.

Figure 12(a) plots the DD predictions of the equilibrium dislocation orientation θ as a function of Burgers vector orientation α, and compares them against the predictions of the line tension model (more details in appendix D). When image stress is correctly accounted for, the DD predictions agree very well with the line tension model. While the line tension model predicts no dependence of θ on the film thickness $2t$, a very weak thickness dependence is observed in DD predictions. The dependence is so weak that it is on the same order of magnitude of the numerical error. If, on the other hand, the image stress is completely ignored, the DD model predicts $\theta = \alpha$, i.e. the dislocation will always be at the screw orientation at equilibrium. This is clearly wrong because it would lead to an infinitely long screw dislocation (parallel to the surface) when $\alpha = 90^\circ$. In contrast, both the DD model with image stress and the line tension model predict that the equilibrium orientation is $\theta = 0^\circ$, i.e. an edge dislocation perpendicular to the surface, which clearly has lower energy. Therefore, this test case shows the importance of accounting for the image stress in DD simulations.

Figure 12(b) compares the MS predictions of the function $\theta(\alpha)$ against the line tension model. The agreement is also good, although the deviation of the MS predictions from the line

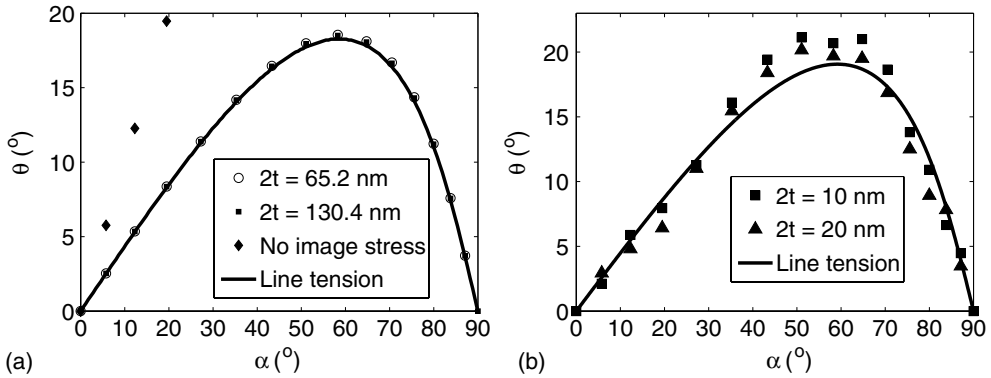

Figure 12. Equilibrium dislocation orientation θ as a function of the Burgers vector orientation α. (*a*) Comparison between DD simulations at two film thicknesses ($2t = 10$ and 20 nm) and the line tension model (which is independent of film thickness). (*b*) Comparison between MS simulations at two film thicknesses ($2t = 10$ and 20 nm) and the line tension model.

tension model is larger than that of the DD predictions. This may be caused by several factors, including (1) the ambiguity in defining the precise location of the dislocation in atomistic simulations and (2) possible angular dependence of dislocation core energy in the atomistic model but absent in the DD and line tension model. Nonetheless, the general agreement among the predictions of the DD, MS and line tension models shows that the most important physical mechanisms controlling the equilibrium dislocation orientation are already accounted for in the DD and line tension models. For example, the surface steps that join the dislocation line at the surface are not considered in the DD and line tension models. As explained in Lothe [36], surface steps are due to core effects that only MD can capture. Surface steps must have a very small effect on the equilibrium dislocation orientation, at least at the length scale considered here.

6. Discussion

The stress field of a dislocation is singular, which is problematic for DD simulations. For our results discussed here, we have generally avoided the singularities, such as by not evaluating the self-stress on the dislocation itself. One method that can be used to eliminate this problem is the non-singular theory of dislocations proposed by Cai *et al* [37].

We have suggested that the boundary problem can be restated using virtual dislocations [8, 17, 23]. However, single (semi-infinite) virtual dislocations at each emerging point are not the only way to solve the problem. For example, Eshelby [38] discussed that a truncated dislocation could be completed by allowing the dislocation to flower out with a spherically symmetric Burger's vector distribution. While this construct may satisfy equilibrium, it introduces further incompatibility to the domain of interest. The idea of a distribution of virtual dislocations could still work, provided that its distribution is confined to the space outside the domain of interest (e.g. the thin film). An example is the dislocation fan on the surface [39]. In comparison, a virtual dislocation tangent to the terminating dislocation seems the easiest to implement and shows the best numerical convergence.

It is interesting to note that our DD simulations, after a careful determination of the image stress fields, predict equilibrium dislocation orientations that are in very good agreement with the much simpler line tension model. For a straight, semi-infinite dislocation intersecting the

surface of an elastic half space, the equilibrium orientation of the dislocation was determined analytically by Yoffe [18] in isotropic elasticity and by Lothe [36] in anisotropic elasticity. Furthermore, Lothe proved the exact solution is identical to that predicted by the line tension model, or equation (D.4). We have also verified this prediction numerically by computing the equilibrium orientation of emerging dislocations in a half space. The DD predictions are identical to those of the line tension model. Since the half space can be considered as a thin film in the limit of $2t \to \infty$, the slight deviation between our thin film and half space results is consistent with the very weak thickness dependence in the thin film results themselves. Therefore, the good agreement in the predictions of equilibrium dislocation orientation in a thin film between the DD and the line tension models can be attributed to the weak thickness dependence of the equilibrium angle. It is worth reporting that, even if the dislocation is confined to a glide plane not orthogonal to the surface, the equilibrium orientation predicted by our DD model (both for thin film and half space) is still in close agreement with the line tension model, even though such constraint was not considered in Lothe's original proof. In this case, the dislocation still experiences a significant (climb) force normal to its glide plane even after it has reached its equilibrium shape.

This paper does not cover all aspects of simulation of dislocations in thin films as we have focused only on the image force. An equally important topic, the mobility of dislocations at free surfaces, is not included but needed to accurately describe dislocation motion near surfaces [40].

7. Summary

We described a complete algorithm to compute the stress field of a dislocation ensemble in a free-standing thin film. We first developed a spectral method to efficiently solve the boundary value problem. We then discussed the necessity of virtual segments when considering emerging dislocations and how the solution is independent of the different choices of virtual segments. The efficiency of computing the image stress for emerging dislocations was enhanced by using the analytical Yoffe image stress solution to cancel the singular stress field. We analyzed the convergence behavior of our numerical methods by comparing with analytic solutions, and demonstrated their self-consistency by comparing the Peach–Koehler force with the numerical derivative of the elastic energy. As a benchmark, we computed the equilibrium orientation of threading dislocations in a free-standing thin film. The predictions from DD, MSs and line tension models all agree well with each other.

Acknowledgments

The work is partly supported by an NSF Career grant CMS-0547681 and an AFOSR/YIP grant. C R Weinberger is supported by a Benchmark Stanford Graduate Fellowship. S Aubry is supported by the Army High Performance Computing Research Center at Stanford. The support of S-W Lee and W D Nix by the Division of Materials Sciences of the Office of Basic Energy Sciences of the US Department of Energy under grant DE-FG02-04ER46163 is appreciated and gratefully acknowledged.

Appendix A. M and N matrices for the half space and thin film

Here we present the explicit expressions for the matrices linking the coefficients A, B, C, E, F, G to the traction vectors and displacement vectors. For a negative half space

the expressions are

$$\boldsymbol{N}^{-} = \begin{bmatrix} 0 & -k_y & \mathrm{i}k_x \\ 0 & k_x & \mathrm{i}k_y \\ \mathrm{i}\dfrac{3\mu+\lambda}{\mu+\lambda} & 0 & k_z \end{bmatrix},$$

$$\boldsymbol{M}^{-} = \begin{bmatrix} -\dfrac{2\mu^2}{\lambda+\mu}k_x & -\mu k_y k_z & 2\mathrm{i}\mu k_x k_z \\ -\dfrac{2\mu^2}{\lambda+\mu}k_y & \mu k_x k_z & 2\mathrm{i}\mu k_x k_z \\ \mathrm{i}\dfrac{2\mu(\lambda+2\mu)}{\lambda+\mu}k_z & 0 & 2\mu k_z^2 \end{bmatrix}.$$

For the positive half space we have

$$\boldsymbol{N}^{+} = \begin{bmatrix} 0 & k_y & \mathrm{i}k_x \\ 0 & -k_x & \mathrm{i}k_y \\ \mathrm{i}\dfrac{3\mu+\lambda}{\mu+\lambda} & 0 & -k_z \end{bmatrix},$$

$$\boldsymbol{M}^{+} = \begin{bmatrix} -\dfrac{2\mu^2}{\lambda+\mu}k_x & -\mu k_y k_z & -2\mathrm{i}\mu k_x k_z \\ -\dfrac{2\mu^2}{\lambda+\mu}k_y & \mu k_x k_z & -2\mathrm{i}\mu k_x k_z \\ -\mathrm{i}\dfrac{2\mu(\lambda+2\mu)}{\lambda+\mu}k_z & 0 & 2\mu k_z^2) \end{bmatrix},$$

and for the thin film

$$\boldsymbol{M}^{\mathrm{S}} = \begin{bmatrix} 2\mu k_x \left(k_z t\cosh(k_z t) - \dfrac{\mu}{\lambda+\mu}\sinh(k_z t)\right) & \mu k_z k_y \sinh(k_z t) & 2\mathrm{i}\mu k_z k_x \sinh(k_z t) \\ 2\mu k_y \left(k_z t\cosh(k_z t) - \dfrac{\mu}{\lambda+\mu}\sinh(k_z t)\right) & -\mu k_z k_x \sinh(k_z t) & 2\mathrm{i}\mu k_z k_y \sinh(k_z t) \\ 2\mathrm{i}\mu \left(\dfrac{\lambda+2\mu}{\lambda+\mu}k_z\cosh(k_z t) - k_z^2 t\sinh(k_z t)\right) & 0 & 2\mu k_z^2\cosh(k_z t) \end{bmatrix},$$

$$\boldsymbol{M}^{\mathrm{A}} = \begin{bmatrix} 2\mu k_x \left(k_z t\sinh(k_z t) - \dfrac{\mu}{\lambda+\mu}\cosh(k_z t)\right) & -\mu k_z k_y \cosh(k_z t) & 2\mathrm{i}\mu k_z k_x \cosh(k_z t) \\ 2\mu k_y \left(k_z t\sinh(k_z t) - \dfrac{\mu}{\lambda+\mu}\cosh(k_z t)\right) & \mu k_z k_x \cosh(k_z t) & 2\mathrm{i}\mu k_z k_y \cosh(k_z t) \\ 2\mathrm{i}\mu \left(\dfrac{\lambda+2\mu}{\lambda+\mu}k_z\sinh(k_z t) - k_z^2 t\cosh(k_z t)\right) & 0 & 2\mu k_z^2\sinh(k_z t) \end{bmatrix},$$

$$\boldsymbol{N}^{\mathrm{S}} = \begin{bmatrix} k_x t \sinh(k_z t) & k_y \cosh(k_z t) & \mathrm{i}k_x \cosh(k_z t) \\ k_y t \sinh(k_z t) & -k_x \cosh(k_z t) & \mathrm{i}k_y \cosh(k_z t) \\ -\mathrm{i}k_z t \cosh(k_z t) + \mathrm{i}\dfrac{(\lambda+3\mu)}{(\lambda+\mu)} \sinh(k_z t) & 0 & k_z \sinh(k_z t) \end{bmatrix},$$

$$\boldsymbol{N}^{\mathrm{A}} = \begin{bmatrix} k_x t \cosh(k_z t) & -k_y \sinh(k_z t) & \mathrm{i}k_x \sinh(k_z t) \\ k_y t \cosh(k_z t) & -k_x \sinh(k_z t) & \mathrm{i}k_y \sinh(k_z t) \\ -\mathrm{i}k_z t \sinh(k_z t) - \mathrm{i}\dfrac{(\lambda+3\mu)}{(\lambda+\mu)} \cosh(k_z t) & 0 & k_z \cosh(k_z t) \end{bmatrix}.$$

Appendix B. Independence of the total stress on the choice of virtual segments

The decomposition of the total stress $\sigma_{ij}^{\mathrm{tot}}$ into the infinite medium stress σ_{ij}^{∞} and the image stress $\sigma_{ij}^{\mathrm{img}}$ is only a technique that helps us find the solution $\sigma_{ij}^{\mathrm{tot}}$, which satisfies the following conditions in domain Ω:

(i) Equilibrium: $\sigma_{ij,j}^{\mathrm{tot}} = 0$ in Ω.
(ii) Zero traction: $\sigma_{ij}^{\mathrm{tot}} n_j = 0$ on surface Γ.
(iii) Domain Ω contains a dislocation population, which can be represented by their Burgers vector distribution: $b_j(\boldsymbol{x})$, $\boldsymbol{x} \in \Omega$.

If domain Ω is simply connected, then the *boundary value problem* that defines $\sigma_{ij}^{\mathrm{tot}}$ has a unique solution. It follows that, no matter how σ_{ij}^{∞} and $\sigma_{ij}^{\mathrm{img}}$ individually are affected by the choice of virtual segments, $\sigma_{ij}^{\mathrm{tot}}$ is unique.

In the following, we clarify this point further by considering two different choices of virtual segments, which lead to two Burgers vector distribution functions, $b_j^1(\boldsymbol{x})$ and $b_j^2(\boldsymbol{x})$ that exist in three-dimensional infinite space $\mathbb{R}^3$. The stress fields of such configurations are uniquely determined by $b_j^1(\boldsymbol{x})$ and $b_j^2(\boldsymbol{x})$ because dislocations in an infinite medium have unique stress fields. By construction, the two dislocation distributions are equivalent inside the domain Ω

$$b_j^1(\boldsymbol{x}) = b_j^2(\boldsymbol{x}) \qquad \boldsymbol{x} \in \Omega$$

and of course both stresses satisfy equilibrium

$$\sigma_{ij,j}^{\infty,1}(\boldsymbol{x}) = \sigma_{ij,j}^{\infty,2}(\boldsymbol{x}) = 0 \qquad \boldsymbol{x} \in \mathbb{R}^3.$$

If we then add on an image stress that satisfies equilibrium to both the above stress fields so that the sum satisfies the zero traction boundary condition defined above (ii), we have

$$\begin{aligned} &\sigma_{ij,j}^{\mathrm{tot},\alpha} = 0 && \text{in} && \Omega \\ &\sigma_{ij}^{\mathrm{tot},\alpha} n_j = 0 && \text{on} && \Gamma \\ &b_j^{\alpha}(\boldsymbol{x}) && \text{is given in} && \Omega \end{aligned}$$

for $\alpha = 1$ or 2 and where $\sigma_{ij}^{\mathrm{tot},\alpha} \equiv \sigma_{ij}^{\infty,\alpha} + \sigma_{ij}^{\mathrm{img},\alpha}$. The consequence of the uniqueness of the boundary value problem defined above is that the two stress fields are equivalent inside the domain Ω.

$$\sigma_{ij}^{\mathrm{tot},1} = \sigma_{ij}^{\mathrm{tot},2} \qquad \boldsymbol{x} \in \Omega$$

Since the dislocation configurations, $b_j^1(\boldsymbol{x})$ and $b_j^2(\boldsymbol{x})$, were not specified outside the domain Ω this must hold for all possible configurations. Since the boundary value problem has a unique solution, $\sigma_{ij}^{\mathrm{tot}}$ does not depend on how the dislocations are continued outside the domain for a simply connected body.

Appendix C. MSs

MSs simulations are applied to compute the equilibrium angle of a dislocation line in a free-standing thin film. We use a method developed by Kurtz [41] and Henager and Hoagland [42] to model a dislocation in a bulk BCC tungsten. The simulation cell consists of a rectangular block of atoms forming a BCC lattice. The block is wider in the x- and y-directions than in the z-direction with an aspect ratio of 3 : 1. The orientation of the BCC lattice relative to the x–y–z coordinate system depends on the angle α of interest. A straight dislocation is introduced at the center of the block along the z-axis, by displacing the atoms according to the dislocation displacement field in an infinite isotropic elastic medium [25]. The Burgers vector is always $\boldsymbol{b} = (a/2)[1\,1\,1]$ (in crystal coordinates). Its angle with the z-axis is determined by the orientation of the BCC crystal. The atomic positions are then relaxed twice using the conjugate gradient algorithm, each time having a different boundary condition. The interatomic interactions are described by the Finnis–Sinclair potential [35] of tungsten. In both relaxations the outmost layer ($\approx$2 nm) of the block in the x- and y-directions is kept fixed. During the first relaxation, periodic boundary conditions are applied along the z-direction. The result is a dislocation in an infinite medium. The dislocation remains parallel to the z-axis due to the boundary condition. The resulting atomistic configuration is used as the initial condition for the second relaxation, in which free surface boundary conditions are applied along the z-axis. Dislocations are observed to rotate away from the initial orientation ($\theta = 0^\circ$) during the second relaxation, unless the initial condition is a perfect screw ($\alpha = 0^\circ$) or a perfect edge ($\alpha = 90^\circ$) dislocation.

After relaxation, atoms with local energy 0.5 eV higher than the cohesive energy are identified as dislocation core atoms. Their positions are fitted to a straight line to determine the equilibrium orientation θ. The equilibrium angle θ is converged with respect to the lateral (i.e. x- and y-) dimension of the simulation cell when the aspect ratio between lateral dimension and film thickness is 3 : 1. Changing the aspect ratio to 4 : 1 does not change the equilibrium angle θ appreciably. The results presented in figure 12(b) are produced from simulation cells containing 900 000 − 2 100 000 atoms, depending on the Burgers vector orientation α.

Figure 11(c) shows a relaxed dislocation structure for the case of $\alpha = 27.2^\circ$. The dislocation line is mostly straight but is slightly curved near the surface, which is likely due to core effects. This curvature of the dislocation near the surface is not systematic in our MS simulations. Several relaxed mixed dislocations do not curve at the surfaces and remain straight across the entire thin film.

Appendix D. Line tension model

Here we describe a simple line tension model, following [36] and [25] (p 151), to predict the equilibrium dislocation orientation in thin films. The equilibrium orientation is the result of a competition between the tendency to minimize the dislocation length L and the tendency to minimize the edge component of the Burgers vector.

Given the geometry in figure 10, and assuming the dislocation line remains straight, the dislocation length is

$$L = \frac{2\,t}{\cos\theta}. \tag{D.1}$$

In isotropic elasticity, the energy per unit length of the dislocation depends on its character angle ϕ, i.e. the angle between the dislocation line and the Burgers vector, $\phi = \theta$–α. A

reasonable line tension model for the energy per unit length of the dislocation is

$$\frac{E}{L} = \frac{\mu(b\sin\phi)^2}{4\pi(1-\nu)}\ln\frac{R}{r_c} + \frac{\mu(b\cos\phi)^2}{4\pi}\ln\frac{R}{r_c}. \tag{D.2}$$

The first term is the self-energy of the edge component of the Burgers vector and the second term is the self-energy of the screw component. R is a large scale cut-off parameter and we will use $R = 2t$ in this work. r_c is a core cut-off parameter and we will use $r_c = b$ here. Therefore, the total energy of the dislocation can be written as

$$E = \left[\frac{\sin^2(\alpha-\theta) + (1-\nu)\cos^2(\alpha-\theta)}{\cos\theta}\right]\frac{\mu b^2 h}{4\pi(1-\nu)}\ln\frac{2t}{b}. \tag{D.3}$$

Given that the terms outside the bracket are constants, the equilibrium angle θ can be obtained by solving the following minimization problem:

$$\min_\theta f(\theta) \equiv \min_\theta \frac{\sin^2(\alpha-\theta) + (1-\nu)\cos^2(\alpha-\theta)}{\cos\theta}. \tag{D.4}$$

For any given α, the equilibrium value of θ can be obtained by solving equation (D.4) numerically. It is clear that the line tension model as described above predicts no dependence of θ on the film thickness.

In the line tension model, the equilibrium angle θ depends only on α and Poisson's ratio ν. Figure 12 plots the function $\theta(\alpha)$ predicted by the line tension model (solid line) for $\nu = 0.28$ (tungsten). When $\alpha = 0^\circ$, $\theta = 0^\circ$, corresponding to a screw dislocation, which also has the shortest possible length. This is obviously the minimum energy state for the dislocation when $\alpha = 0^\circ$. As α increases, θ initially increases in the same direction as α because the dislocation has a tendency to stay close to the screw orientation. However, as α increases beyond 60°, θ starts to decrease. When $\alpha = 90^\circ$, $\theta = 0^\circ$, corresponding to an edge dislocation, which has the shortest possible length. In this case, the tendency of the dislocation to be as short as possible is the dominant mechanism that determines the equilibrium orientation of the dislocation.

References

[1] Devincre B and Kubin L P 1997 Mesoscopic simulations of dislocations and plasticity *Mater. Sci. Eng.* A **234–236** 8–14

[2] Schwarz K W 1999 Simulation of dislocations on the mesoscopic scale: I. Methods and examples *J. Appl. Phys.* **85** 108–19

[3] Ghoniem N M and Sun L Z 1999 Fast-sum method for the elastic field of three-dimensional dislocation ensembles *Phys. Rev.* B **60** 128–40

[4] Cai W, Bulatov V V, Peirce T G, Hiratani M, Rhee M, Bartelt M and Tang M 2004 Massively-parallel dislocation dynamics simulations *Solid Mechanics and Its Applications* vol 115 (Dordrecht: Kluwer) p 1

[5] Bulatov V, Cai W, Fier J, Hiratani M, Hommes G, Pierce T, Tang M, Rhee M, Yates K and Arsenlis T 2004 Scalable line dynamics in *ParaDis Proc. 2004 ACM/IEEE Conf. on Supercomputing (PA, USA, November 2004)* p 19

[6] Arsenlis A, Cai W, Tang M, Rhee M, Oppelstrup T, Hommes G, Pierce T G and Bulatov V V 2007 Enabling strain hardening simulations with dislocation dynamics *Modelling Simul. Mater. Sci. Eng.* **15** 553

[7] Weygand D, Friedman L H, van der Giessen E and Needleman A 2001 Discrete dislocation modeling in three-dimensional confined volumes *Mater. Sci. Eng.* A **309–310** 420–24

[8] Weygand D, Friedman L H, Van der Giessen E and Needleman A 2002 Aspects of boundary-value problem solutions with three-dimensional dislocation dynamics *Model. Simul. Mater. Sci. Eng.* **10** 437–68

[9] Nix W D 1989 Mechanical properties of thin films *Metall. Trans.* **20A** 2217–45

[10] Dehm G, Wagner T, Balk T J, Arzt E and Inkson B J 2002 Plasticity and interfacial dislocation mechanisms in epitaxial and polycrystalline al films constrained by substrates *J. Mater. Sci. Technol.* **18** 113–17

[11] Pant P, Schwarz K W and Baker S P 2003 Dislocation interactions in thin fcc metal films *Acta Mater.* **51** 3243–58

[12] von Blanckenhagen B, Gumbsch P and Arzt E 2003 Dislocation sources and the flow stress of polycrystalline thin metal films *Phil. Mag. Lett.* **83** 1–8
[13] Uchic M D, Dimiduk D M, Florando J N and Nix W D 2004 Sample dimensions influence strength and crystal plasticity *Science* **305** 986–9
[14] Nicola L, Xiang Y, Vlassak J J, van der Giessen E and Needleman A 2006 Plastic deformation of freestanding thin films: Experiments and modeling *J. Mech. Phys. Solids* **54** 2089–110
[15] Shan Z W, Mishra R K, Syed Asif S A, Warren O L and Minor A M 2008 Mechanical annealing and source-limited deformation in submicrometre-diameter Ni crystals *Nature Mater.* **7** 115–19
[16] Weinberger C R and Cai W 2007 Computing the image stress in an elastic cylinder *J. Mech. Phys. Solids* **55** 2027–54
[17] Deng J, El-Azab A and Larson B C 2008 On the elastic boundary value problem of dislocations in bounded crystals *Phil. Mag.* **88** 3527–48
[18] Yoffe E H 1961 A dislocation at a free surface *Phil. Mag.* **6** 1147
[19] Eshelby J D 1979 Boundary Problems *Dislocations in Solids* vol 1 (Amsterdam: North-Holland) p 167
[20] Hartmaier A, Fivel M C, Canova G R and Gumbsch P 1999 Image stresses in a free standing thin film *Modelling Simul. Mater. Sci. Eng.* **7** 781–93
[21] Barber J R 2002 *Elasticity* 2nd edn (Dordrecht: Kluwer)
[22] Bulatov V V and Cai W 2006 *Computer Simulations of Dislocations* (Oxford: Oxford University Press)
[23] Liu X H and Schwarz K W 2005 Modelling of dislocations intersecting a free surface *Modelling Simul. Mater. Sci. Eng.* **13** 1233–47
[24] Li J C M 1964 Stress field of a dislocation segment *Phil. Mag.* **5** 1097–8
[25] Hirth J P and Lothe J 1982 *Theory of Dislocations* (Malabar, FL: Krieger)
[26] Tang M, Cai W, Xu G and Bulatov V 2006 A hybrid method for computing forces on curve dislocations intersecting free surfaces in three–dimensional dislocation dynamics *Modelling Simul. Mater. Sci. Eng.* **14** 1139–51
[27] Bastecka J 1964 Interaction of dislocation loop with free surface *Czech. J. Phys.* **14B** 430–42
[28] Tang M 2008 *private communication*
[29] Korner A, Svoboda P and Kirchner H O K 1977 Finite dislocation elements in finite media: I. Basic theory *Phys. Status Solidi* b **80** 441–50
[30] Korner A, Karnthaler H P and Kirchner H O K 1977 Finite dislocation elements in finite media: II. Trapezoidal splitting of partial dislocations in thin foils *Phys. Status Solidi* b **81** 191–98
[31] Hazzledine B M, Karnthaler H P and Wintner E 1975 Non-parallel dissociation of dislocations in thin foils *Phil. Mag.* **32** 81–97
[32] Mills M J and Stadelmann P 1989 A study of the structure of Lomer and 60° dislocations in aluminium using high-resolution transmission electron microscopy *Phil. Mag.* A **60** 355–84
[33] Mills M J, Daw M S and Foiles S M 1994 High-resolution transmission electron microscopy studies of dislocation cores in metals and intermetallic compounds *Ultramicroscopy* **56** 79–93
[34] Aubry S and Hughes D 2006 Reductions in stacking faults width in fcc metals: empirical calculations *Phys. Rev.* B **73** 1–15
[35] Finnis M and Sinclair E 1984 A simple empirical n-body potential for transition metals *Phil. Mag.* A **50** 45–55
[36] Lothe J 1970 The image force on dislocations at free surfaces—comments on the concept of line tension *Natl. Bur. Stand. Spec. Publ.* **317** 11–20
[37] Cai W, Arsenlis A, Weinberger C R and Bulatov V V 2006 A non-singular continuum theory of dislocations *J. Mech. Phys. Solids* **54** 561
[38] Eshelby J D and Laub T 1967 The interpretation of terminating dislocations *Can. J. Phys.* **45** 887–92
[39] Belov A Yu 1992 Dislocations emerging at planar boundaries *Elastic Strain Fields and Dislocation Mobility* (Amsterdam: Elsevier) pp 391–446 chapter 6
[40] Weinberger C R and Cai W 2008 Surface-controlled dislocation multiplication in metal micropillars *Proc. Natl. Acad. Sci. USA* **105** 14304
[41] Kurtz R J 1997 *Computer simulation of extrinsic grain boundary defects PhD Thesis* Washington State University
[42] Henager C H and Hoagland R G 2004 Dislocation core fields and forces in fcc metals *Scr. Mater.* **50** 1091–5